scientific reports

Check for updates

OPEN

A multifaceted examination of the action of PDE4 inhibitor rolipram on MMP2/9 reveals therapeutic implications

Arka Bagchi[1], Analabha Roy[2]✉, Anindya Halder[3] & Arunima Biswas[1]✉

A PDE4 (phosphodiesterase 4) inhibitor, Rolipram, was previously found to down-regulate (in a manner dependent on cAMP (cyclic adenosine monophosphate)-PKA (protein kinase A)) MMP2 (matrix metalloproteinase 2) and MMP9 protein expression levels, important markers of epithelial-to-mesenchymal transition in human breast cancer cell lines. However, zymographic studies revealed that rolipram could also alter the enzymatic activities of these MMPs, even in the presence of the PKA inhibitor H89. This calls for more detailed investigations of the inhibitory mechanism of rolipram on MMP2 and MMP9. The prediction of ligand-based targets through online reverse screening indicated that proteases are likely targets of rolipram. Computational molecular docking also demonstrated significant binding affinities of rolipram for both MMP2 and MMP9 proteins. Concurrently, a well-known inhibitor of MMPs, SB3CT, was utilized as a positive control for this study. The best models of the docked complexes were used as initial conditions for molecular dynamics (MD) simulations to explore their dynamic behavior and stability. In particular, both the MMP2-rolipram and MMP9-rolipram complexes were found to be stable and compact for the duration of the simulation ($500\ ns$). Several stable hydrogen bonds were also detected between the proteins and rolipram. *In vitro* experiments using primary cells from patients with breast cancer also showed that rolipram could alter the enzymatic activities of MMP2 and MMP9, independent of the cAMP-PKA signaling pathway, though it was thought to be cAMP-PKA dependent previously. These observations indicate the ability of rolipram to control breast cancer by regressing the functions of MMP2 and MMP9, thus having 'off-targets' other than PDE4 to have direct control over proteins that are involved in the advancement of metastasis.

Keywords MMP2, MMP9, PDE4, Rolipram

The complex and multistage cancer invasion and metastasis process is characterized by numerous genetic alterations. A crucial element in this progression is the breakdown of the extracellular matrix[1]. Matrix metalloproteinases (MMPs), a group of zinc-dependent endopeptidases with the ability to break down components of the extracellular matrix, play a significant role in facilitating cancer invasion and metastasis[2,3]. Increased concentrations of specific MMPs can be identified in tumor tissue or serum of individuals with advanced cancer[4,5], therefore, their potential as prognostic markers in cancer has been extensively studied. In addition, the expressions of MMP2 and MMP9, which are characterized as gelatinases, have been implicated in the progression and metastasis of breast cancer. Both MMPs are known to be differentially expressed in breast tumor tissues compared to adjacent normal tissues[6]. The overexpression of MMP2 and MMP9 was also associated with poor overall survival in patients with breast cancer, as well as higher histological grades, greater tumor size, and metastases[7]. MMP2[8] and MMP9[9] were also found to be responsible for the modulation of the immune response in the microenvironment of breast tumors. Therefore, several attempts have been made by researchers to functionally inhibit the activities of these MMPs to antagonize the progression and metastasis of breast cancer.

[1]Cell and Molecular Biology Laboratory, Department of Zoology, University of Kalyani, Kalyani, Nadia, West Bengal 741235, India. [2]Department of Physics, The University of Burdwan, Bardhaman, West Bengal 713104, India. [3]Department of General Surgery, All India Institute of Medical Sciences, Kalyani, West Bengal 741250, India. ✉email: daneel@utexas.edu; aroy@phys.buruniv.ac.in; arunima10@gmail.com; arunima10@klyuniv.ac.in

Rolipram, a specific phosphodiesterase 4 (PDE4) inhibitor that functions as an antidepressant, was approved for use on the market, but later the drug was returned to the clinical trial due to adverse effects such as nausea and vomiting. However, several

other PDE 4 inhibitors such as roflumilast, crisaborole, and apremilast were synthesized [10] which passed the clinical trials and were on the market after FDA approval. Although some adverse effects of rolipram in a narrow concentration range persisted, the drug made considerable advances in terms of the benefit-to-risk ratio. Over a period of time the search and synthesis of second-generation PDE4 inhibitors went on, several new inhibitors were synthesized and still today the research to have new PDE4 inhibitors is active. This brings in new preclinical compounds that are entering clinical trials. Like PDE inhibitors, there is significant research on MMP inhibitors, with some reaching clinical trials as early as the 1990s, such as marimastat and ilomastat / GM6001. Because these drugs were zinc-binding, they could inhibit several MMPs. However, these drugs did not show much promise in clinical trials as there were significant and adverse side effects associated with the use of drugs in patients. Since these inhibitors are associated with a certain amount of non-specificity compared to the available PDE4 inhibitors on the market, where specificity is not an issue, the search for MMP inhibitors with better specificity is still on.

In a previous study, it was shown that the PDE4 inhibitor rolipram was able to alter the fate of the hedgehog signaling pathway in both the hormone-responsive breast cancer cell line MCF-7 and the triple-negative breast cancer cell line (TNBC) MDA-MB-231 in a cAMP-PKA-dependent manner[11]. Rolipram, a specific PDE4 inhibitor, is one of the most studied PDE4 inhibitors and is chemically a 4-substituted pyrrolidinone. Several analogues of this inhibitor have been synthesized to understand rolipram itself, and a variety of analogues of this molecule have been studied to evaluate the structural requirements of the potency of the PDE4 inhibitor. Furthermore, rolipram was also observed to modulate the PTEN-PI3K-Akt axis in breast cancer cell lines[11]. Modulations of these pathways resulted in a successful down-regulation of MMP2 and MMP9 expression, along with other epithelial to mesenchymal transition (EMT) markers such as E-cadherin and vimentin in breast cancer cell lines. Concomitant retardations in the wound healing capabilities of both cell lines were also evident[12]. Since MMP2 and MMP9 expressions cannot justify their activities, the objective of this work has been to analyze the effect of rolipram on the enzymatic activities of these MMPs and to understand whether the mechanism of action of rolipram on MMP2 and MMP9 is always dependent on cAMP-PKA, as speculated in previous studies[12].

The aforementioned study already predicted rolipram as an anti-breast cancer agent that can be exploited in combination with existing chemotherapeutic drugs to curb chemoresistance and tumor relapse. Hence, rolipram has been considered for drug repurposing to offer a shorter path in drug discovery for breast cancer. Although rolipram traditionally targets the phosphodiesterase 4 isoform, due to the intrinsic complexity of the molecular structure, drugs such as rolipram have the potential and practical interaction possibilities with several targets, which can be termed as "off-targets", either in a particular signaling cascade or in different cascades. This idea of polypharmacology has changed the idea of drug design from having one target protein in a disease to having multiple target proteins for better efficacy. Hence, targeting druggable proteins might lead to the identification of novel off-target interactions, leading to a successful focus on drug repurposing. Additionally, the *in silico* prediction of ligand-protein interactions would reduce and refine the excessive budget of the laboratory processes significantly.

Results

Enzymatic activity of MMP2 and MMP9 in presence of rolipram

To assess the modulation of the enzymatic activities of MMP2 and MMP9 in MCF-7 and MDA-MB-231 cell lines, gelatin zymography of the conditioned culture medium was performed. MCF-7 and MDA-MB-231 cells were treated with respective doses IC_{50} of 40 μM and 53 μM rolipram, which were determined in the previous study[12]. The data obtained from the study revealed that the activities of both MMP2 and MMP9 were significantly down-regulated by rolipram treatment. To observe whether the activities of these enzymes depend on cAMP-PKA, MCF-7 and MDA-MB-231 cells were treated with H89 (10 μM), a PKA inhibitor[11]. It was evident from the zymography that H89 did not significantly inhibit the activity of both MMPs. However, there was significant inhibition of MMP2 and MMP9 activities after cotreatment with rolipram and H89, indicating a modulation of MMP proteins independent of cAMP-PKA (Fig. 1A).

Determination of possible off-targets of rolipram

As rolipram showed an inhibitory effect on MMP2 and MMP9 even in the presence of H89 in both hormone-responsive and triple-negative breast cancer cell lines, determining the mode of action of rolipram on MMP2 and MMP9 was of key importance. Therefore, it was crucial to identify possible off-targets of rolipram, which may mediate inhibitory effects even in the presence of H89. Furthermore, previous data obtained from gelatin zymography also raised the question of a possible direct interaction between rolipram and MMP proteins, bypassing the cAMP-PKA signaling pathway. Data obtained from the SwissTargetPrediction server revealed that 6.7% of the total probable targets for rolipram consist of proteases, along with 40% comprising phosphodiesterases (Fig. 1B, Table T1). This information led to the investigation of whether there are potential interactions between these MMPs and rolipram or not.

Prediction of MMP2-rolipram and MMP2-SB3CT interactions

Molecular docking studies were performed to predict the potential interaction between rolipram and MMP2. In this study, 2-[(4-phenoxyphenyl)sulfonylmethyl]thiirane (SB3CT), a well-known inhibitor of MMP2 and MMP9 available on the market, was also analyzed as a positive control. To select the model structure for this study, all available molecular structures from the RCSB database were compiled to perform molecular docking

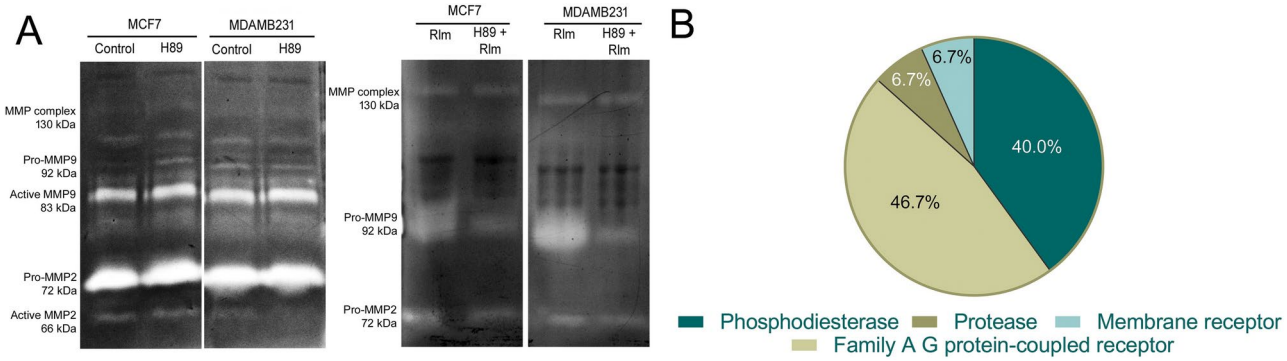

Fig. 1. (**A**) Gelatin zymography of culture media conditioned with MCF-7 and MDA-MB-231 cells. The cells were treated with H89, rolipram (Rlm), and H89-rolipram for 24 $hours$. Images of the full-length gels are available at Fig. S1 (**B**) Percentages of predicted probable protein targets (from *Homo sapiens*) of rolipram obtained from the SwissTargetPrediction server.

with rolipram, the details of which are available in Table T2. The final model for MMP2 (PDB ID: 1CK7) was selected based on two key criteria: a fully intact protein structure,

including zinc ions and the catalytic domain, and the structure that exhibits the highest binding affinity with rolipram. The dimensions of the ligand binding search box in the docking studies were determined based on the molecular structure of 7XGJ (biological assembly 1). This structure represents the crystal form of the MMP2 catalytic domain with an inhibitor, showing the highest docking affinity among the available models when the inhibitor was replaced with rolipram. The search box for this docking (a 35Å$\times$ 35Å$\times$ 35Å cube centered on the zinc ions) was transcluded into the docking sessions with rolipram/SB3CT and the final selected model (PDB ID: 1CK7)[13].

The most favorable model obtained from Autodock was analyzed for each complex, MMP2 -rolipram and MMP2 - SB3CT (as a control). The best MMP2-rolipram model showed a binding affinity of $-8.32\ kcal/mol$. Further analysis revealed two potential conventional hydrogen bonds between rolipram and histidine (HIS) at the 193^{rd} residue, as well as a hydrogen bond with aspargine (ASN) at the 55^{th} residue of MMP2. Furthermore, van der Waals interactions between rolipram and

MMP2 were observed at the following sites: tyrosine (TYR) in the 182^{nd} residue, phenylalanine (PHE) in the 184^{th} and 195^{th} residues, glycine (GLY) in the 103^{rd}, proline (PRO) in the 105^{th} and 183^{rd} residues, and ASN in the 104^{th} residue (Fig. 2 A). In the control simulation, the best model of the MMP2-SB3CT complex exhibited a binding affinity of $-7.65\ kcal/mol$. This complex did not show conventional hydrogen bond between SB3CT and the protein, but several van der Waals interactions with the 105^{th} PRO, 104^{th} and 111^{th} ASN, 182^{nd} TYR and 103^{rd} GLY residues (Fig. 2 B). Therefore, it can be inferred that rolipram may interact with MMP2 as effectively as SB3CT.

Stability and integrity analysis of MMP2-rolipram and MMP2-SB3CT complexes

To further investigate the stability of the MMP2-rolipram and MMP2-SB3CT complexes, molecular dynamics (MD) simulations were performed on the best model complexes obtained from molecular docking. Furthermore, a simulation of the free MMP2 protein was conducted without ligands to study its dynamics. Simulations were performed in triplicate for $500\ nanoseconds\ (ns)$ to examine the stability and dynamic behavior of these complexes over time.

During simulations, the initial configuration showed that the rolipram molecule in the MMP2-rolipram complex relocated to an alternative binding pocket in MMP2 before achieving stability (Fig. 2A and C). In contrast, the SB3CT molecule in the MMP2-SB3CT complex shifted to an adjacent binding pocket in MMP2 at the end of the simulation (Figs. 2B and D). Analysis of the root-mean-square deviation (RMSD) revealed that the free MMP2 protein stabilized with an RMSD of $0.45\ nm$ from its initial configuration. In contrast, the MMP2-rolipram complex stabilized at a higher RMSD of $0.7\ nm$, while the MMP2-SB3CT complex achieved stability with an RMSD of $0.4\ nm$ from its initial configuration (Fig. 3A and C, top panel). Examination of the radius of gyration (R_g) indicated that the MMP2 protein maintained its compactness in the presence of both ligands and in its free form. The MMP2-rolipram complex preserved most of its initial compactness until the end of the simulation, similar to the MMP2-SB3CT simulation. Interestingly, the free MMP2 simulation exhibited even greater stability in R_g at 2.8 within the same simulation time (Fig. 3A and C, middle panel). Further analysis of root-mean-square fluctuation (RMSF) of specific amino acid residues in these complexes, compared to the free MMP2 simulation, provided insights into possible structural changes of the MMP2 protein due to its interactions with ligands. Significant fluctuations of approximately $0.2\ nm$ were observed in both simulations in the amino acid residues in MMP2 corresponding to its catalytic domain (Fig. 3B and D).

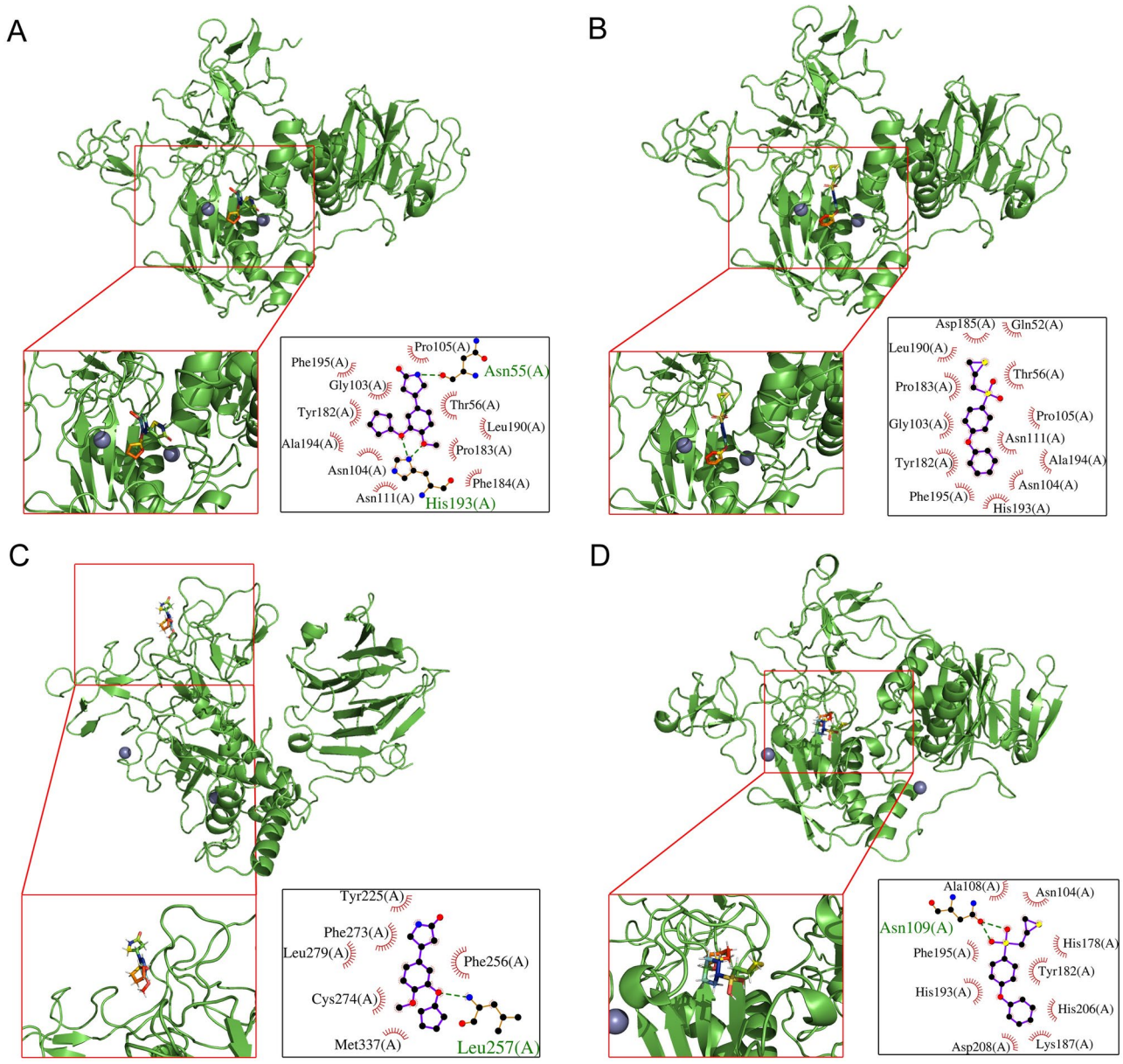

Fig. 2. The most favorable docked complexes of MMP2-rolipram (panel (**A**)) and MMP2-SB3CT (panel (**B**)). Snapshots of the MMP2-rolipram complex (panel (**C**)) and the MMP2-SB3CT complex (panel (**D**)), at the end of the 500 ns (nanosecond) MD simulation. The insets in the lower right display of each panel show two-dimensional diagrams of the predicted interactions of the respective poses, where the predicted hydrogen bonds are shown in green.

Identification and analysis of stability of hydrogen bonds involving rolipram and SB3CT with MMP2

The analysis of hydrogen bond formation between MMP2 and ligands (rolipram and SB3CT) was performed using MDTraj[14]. This Python module utilizes the Baker-Hubbard method to identify hydrogen bonds in the simulation trajectories. According to this criterion, a hydrogen bond of the type $d-h\cdots a$ (donor, hydrogen, and acceptor, respectively) is detected whenever the cut-off distance $r_{ha} < 0.25\ nm$ and the angle $\theta_{dha} > 2\pi/3$ (120°). The analysis revealed several hydrogen bonds for the MMP2-rolipram simulation (Fig. 3A, bottom panel). However, a more detailed analysis of the r_{ha} and θ_{dha} of these identified hydrogen bonds revealed that only two of them occurred at a frequency greater than 10%, namely, one $N-H\cdots O$ bond and one $N-H\cdots O_1$, both involving the 257^{th} LEU residue (Fig. S2). In the control simulation with SB3CT, three hydrogen bonds with similar occurrences were identified: two involving the 104^{th} ASN residue of MMP2 (of the types $N-H\cdots O_{1,2}$) and one of the type $N-H\cdots O_1$ involving the 109^{th} ASN residue (Fig. S3).

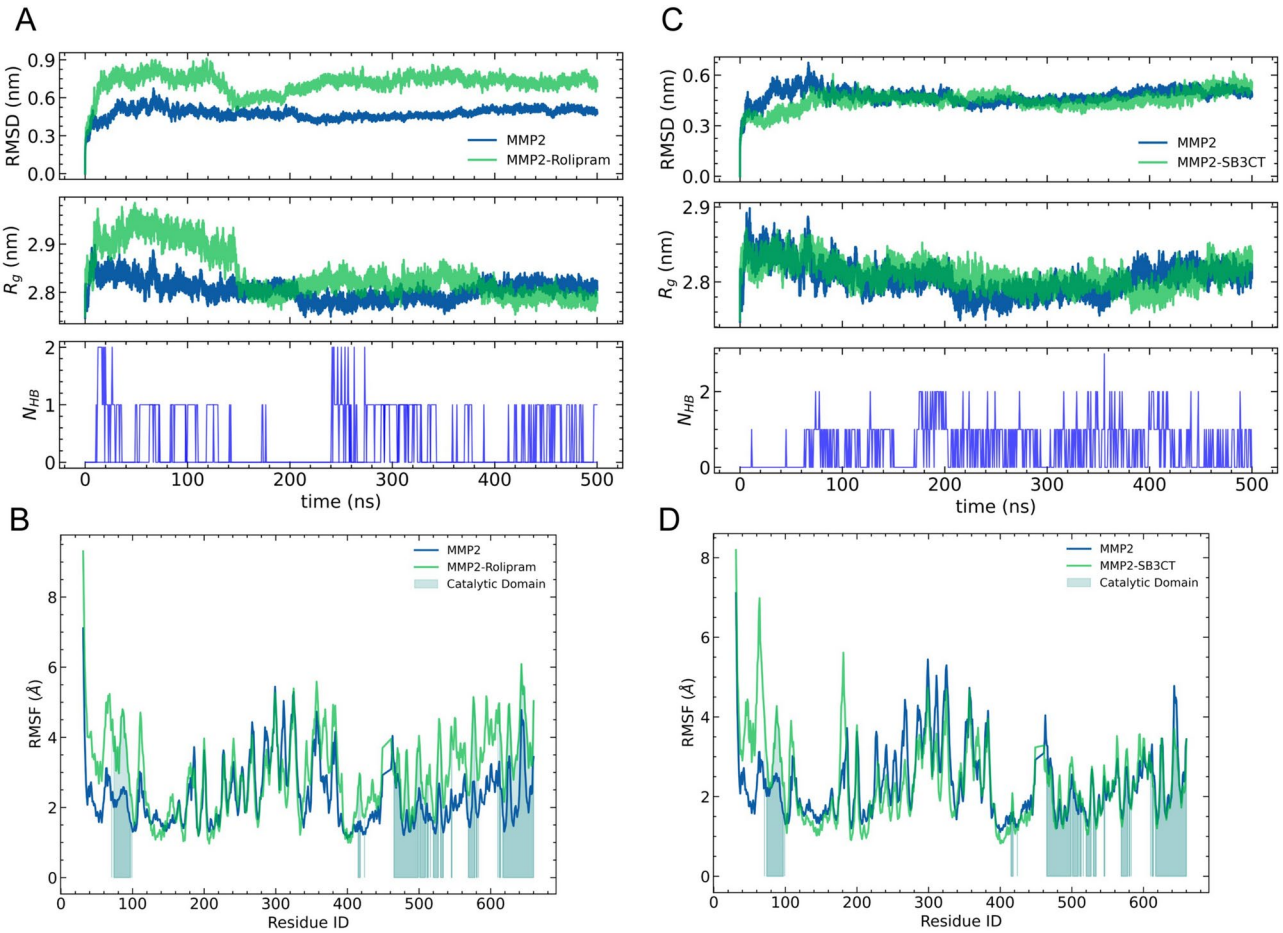

Fig. 3. First row at the top: plots of root-mean square deviation (RMSD) versus time of the free MMP2, MMP2-rolipram complex (panel (**A**)), and MMP2-SB3CT complex (panel (**C**)). Second row: plots of radius of gyration (R_g) of MMP2-rolipram complex (panel (**A**)) and MMP2-SB3CT complex (panel (**C**)) along with free MMP2. Third row at the bottom: number of hydrogen bonds formed during the 500 ns simulation period between MMP2 and rolipram (panel (**A**)) as well as MMP2 and SB3CT (panel (**C**)), analyzed by MDTraj. The RMSF plots of MMP2-rolipram complex (panel (**B**)) and MMP2-SB3CT complex (panel (**D**)) in comparison with free MMP2. In each RMSF plot, the shaded portions represent the catalytic domain of the MMP2 protein.

Principal component analysis of MMP2-rolipram and MMP2-SB3CT complexes

Principal component analysis (PCA) was performed to analyze the dynamics of the MMP2-rolipram and MMP2-SB3CT complexes with backbone, ligand, and Zinc ion selections. Detailed methodologies for PCA are outlined in Section Molecular dynamic simulation. The PCA results for the MMP2-rolipram complex showed that the first two principal components (PC_1 and PC_2) accounted for 80% of the total variance in the data. The free-energy landscape along the principal components $PC_{1,2}$ showed a clear separation between the two metastable states, with the global minimum at the end of the trajectory (Fig. 4). The cross-section of the landscape along a co-ordinate ϕ showed dominant contributions from a clear asymmetric double-well potential, with the metastable minimum at the beginning of the trajectory, and the global minimum at the end. The free-energy estimates at the two minima are also indicated in the plot. A rough estimate of the change in free energy as the system transitions from the initial to the final equilibrium configuration is $\Delta G \approx -2.03\ kcal \cdot mol^{-1}$. Adding this to the initial affinity at the docked pose ($\Delta G \approx -8.32\ kcal \cdot mol^{-1}$) yields an estimate of $\Delta G \approx -10.35\ kcal \cdot mol^{-1}$ for the net change in free energy.

The PCA results for the MMP2-SB3CT complex showed that the first two principal components accounted for 85% of the total variance in the data. The free-energy landscape along the principal components $PC_{1,2}$ showed a clear separation between the metastable state at the beginning and the global minimum at the end of the trajectory (Fig. 5). The cross-section of the landscape along a co-ordinate ϕ showed a clear double-well potential, with the global minimum at the end of the trajectory. The free-energy estimates at the two minima were also indicated in the plot, revealing a net change in free energy of $\Delta G \approx -1.47\ kcal \cdot mol^{-1}$ as the system transitions from the initial to the final equilibrium configuration. Adding this to the initial affinity at the docked pose ($\Delta G \approx -7.65\ kcal \cdot mol^{-1}$) yields an estimate of $\Delta G \approx -9.12\ kcal \cdot mol^{-1}$ for the net change in free energy. In comparison of the two cases, the MMP2-rolipram complex showed a much lower net change

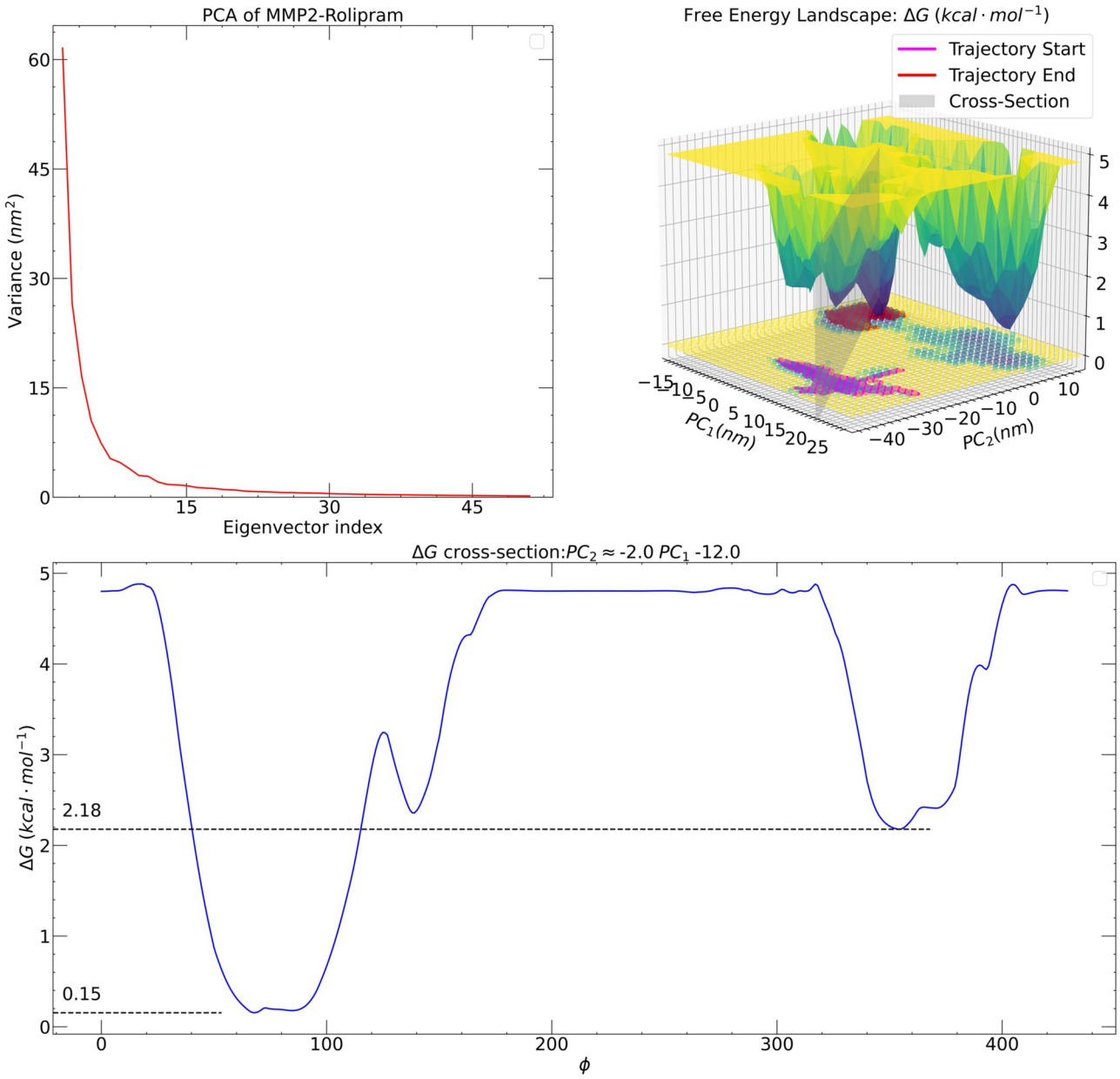

Fig. 4. Principal Component Analysis (PCA) results for the MMP2-rolipram complex. The top left panel displays the variance (eigenvalues) obtained from diagonalizing the covariance matrix in Eq. 1, plotted against the eigenvector index and sorted in decreasing order. The top right panel shows the free-energy landscape, which represents the bidimensional projections of the free-energy along the principal components $PC_{1,2}$. The PCA data is visualized as a yellow-green density plot on the $PC_{1,2}$ plane, together with projections of the concatenated trajectory as indicated in the legend. The bottom panel provides a cross-section of the landscape along a co-ordinate ϕ, chosen to vary along a line (equation specified in the title) that includes both the metastable minimum at the start of the trajectory and the global minimum at the end. Additionally, the free-energy estimates (in $kcal \cdot mol^{-1}$) at the two minima are indicated.

in free energy than the MMP2-SB3CT complex. This suggests that the MMP2-rolipram complex is more stable than the MMP2-SB3CT complex, indicating better binding of rolipram to MMP2 than SB3CT.

Prediction of MMP9-rolipram and MMP9-SB3CT interactions

Docking studies between rolipram and MMP9 (PDB id: 1L6J) were initially carried out following a methodology similar to that for MMP2 as described in Section Prediction of MMP2-rolipram and MMP2-SB3CT interactions. The details of all molecular structures of MMP9 available in the RCSB database and the respective results of the docking studies are available in Table T3. Structures with poor experimental metrics were not considered for the docking studies. The search box for ligand binding was centered on the zinc atoms (residue ID: 500 and 501) of the MMP9 protein and set to dimensions 17Å× 17Å× 17Å. This ensured that it encompassed the catalytic

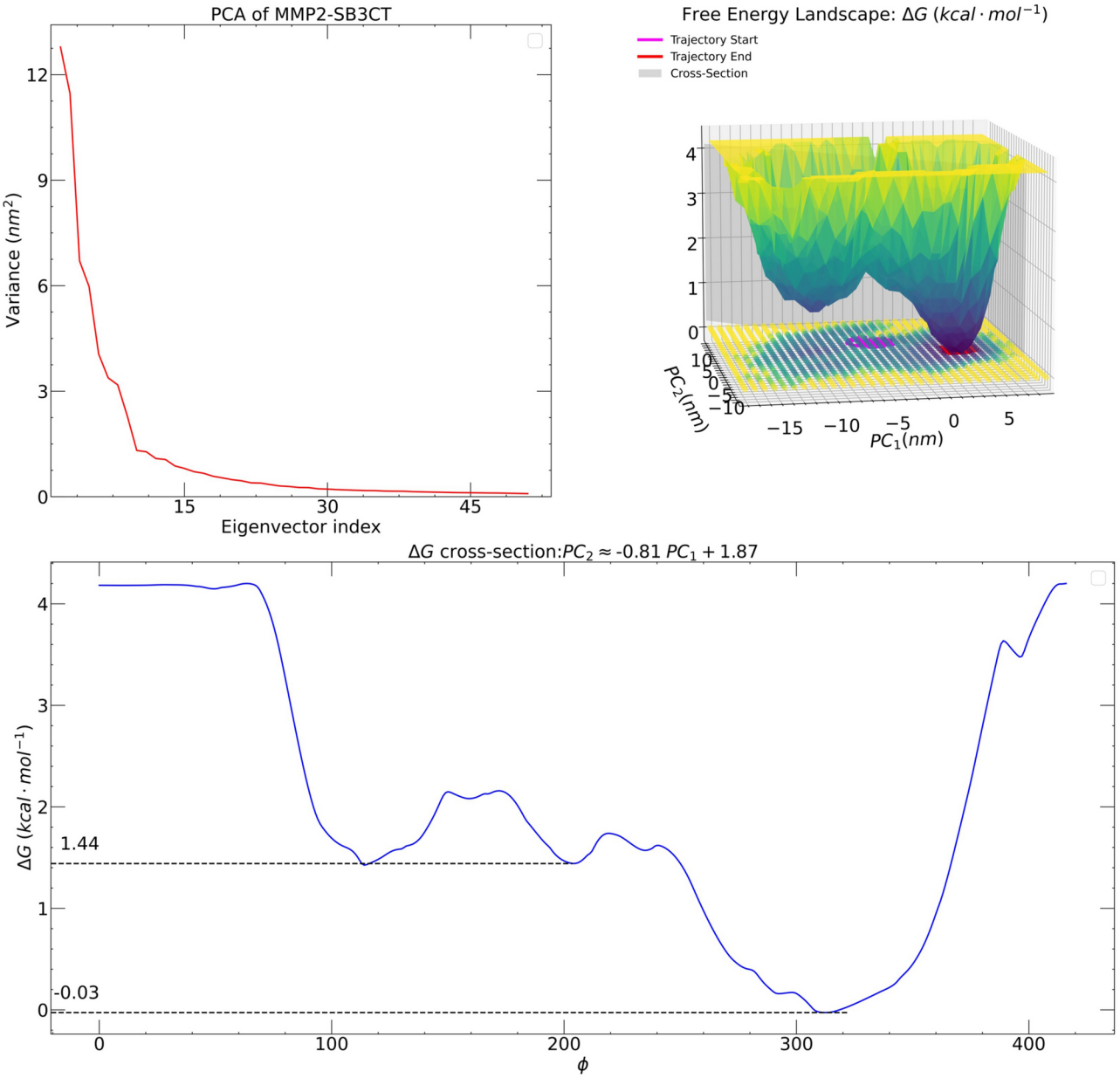

Fig. 5. PCA results for the MMP2-SB3CT complex showing eigenvalues plotted against eigenvector index in the top left panel. The top right panel shows the free energy landscape along the principal components in a manner similar to the corresponding panel in Fig. 4. The bottom panel shows the cross-section of the landscape along the ϕ co-ordinate. The free energy estimates at the two minima are also indicated in $kcal \cdot mol^{-1}$.

domain [15]. This search box also housed the 401^{st} HIS, 402^{nd} GLU, 405^{th} HIS, and 411^{th} HIS residues, which are considered the catalytic triad of MMP9. The analysis indicated that the most favorable MMP9-rolipram complex had a binding affinity of $-10.11\ kcal/mol$. Examination of the MMP9-rolipram complex model for protein-ligand interaction revealed the presence of three potential

hydrogen bonds: one between rolipram and the 188^{th} LEU residue of MMP9, and the others with the 402^{nd} GLU and 424^{th} ARG residues (see Fig. 6A). In the control docking with similar search box parameters, the best MMP9-SB3CT complex displayed a binding affinity of $-10.21\ kcal/mol$, although only a conventional hydrogen bond involving 424^{th} ARG was predicted between the two entities. Moreover, several non-bonding van der Waals interactions were observed in both predicted interactions involving rolipram, SB3CT, and MMP9 (see Fig. 6B).

Stability and integrity analysis of MMP9-rolipram and MMP9-SB3CT complexes

The stability of MMP9 interactions with rolipram and the SB3CT control ligand was examined by MD simulations *in silico*, using parameters similar to those of MMP2 and ligands detailed in Section Stability and integrity

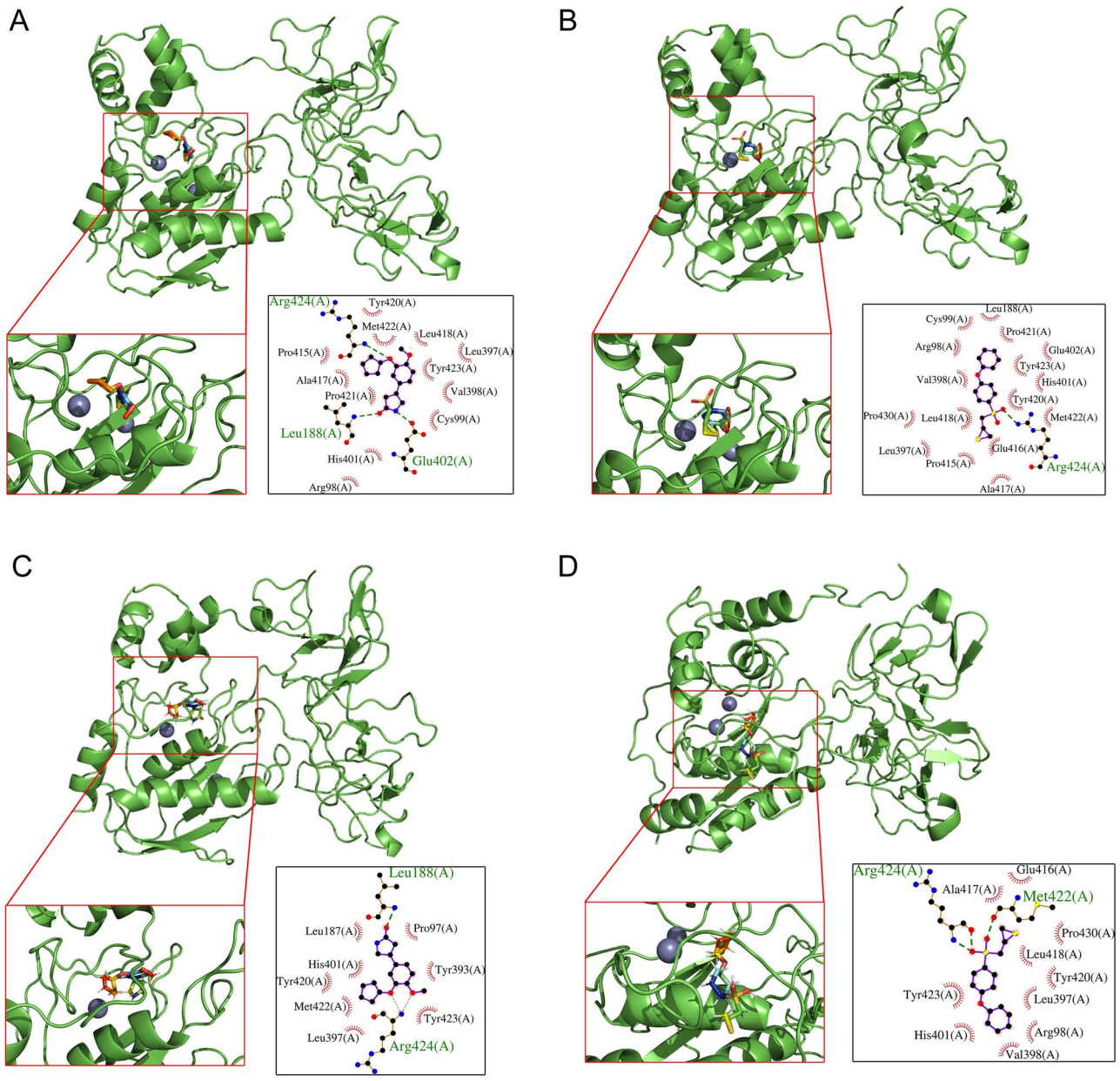

Fig. 6. The most favorable docked complexes of MMP9-rolipram (panel (**A**)) and MMP9-SB3CT (panel (**B**)). Snapshots of the MMP9-rolipram complex (panel (**C**)) and the MMP9-SB3CT complex (panel (**D**)), at the end of the 500 ns (nanosecond) MD simulation. The insets in the lower right display of each panel show two-dimensional diagrams of the predicted interactions of the respective poses, where the predicted hydrogen bonds are shown in green.

analysis of MMP2-rolipram and MMP2-SB3CT complexes. The MMP9-rolipram complex that exhibited the most favorable docking was selected as the starting point of the simulation.

Comparison of the molecular pose after 500 ns simulation with the initial configuration showed that the rolipram molecule stayed in the same binding pocket throughout and achieved stability (Fig. 6A and C). In the control simulation, the SB3CT molecule was also observed to stabilize within the same binding site (Fig. 6B and D). The simulation involving free MMP9 appeared to stabilize at an RMSD of 4.5 nm from the beginning of the simulation. In the simulation of the MMP9-rolipram complex, the protein stabilized at an RMSD of 4 nm, while the MMP9-SB3CT complex stabilized at an RMSD of 3.8 nm (Fig. 7A and C, top panel).

Analysis of the R_g plots of the complexes and free MMP9 showed comparable results for both ligands (Fig. 7A and C, middle panel). Examining residue-specific RMSF indicated that both ligands induced notable differences in the catalytic domain residues (to the tune of $1-2$ Å) compared to the corresponding values in the free protein. Fluctuations outside this domain were minor and restricted to the residue range $340-390$ (Fig. 7B and D).

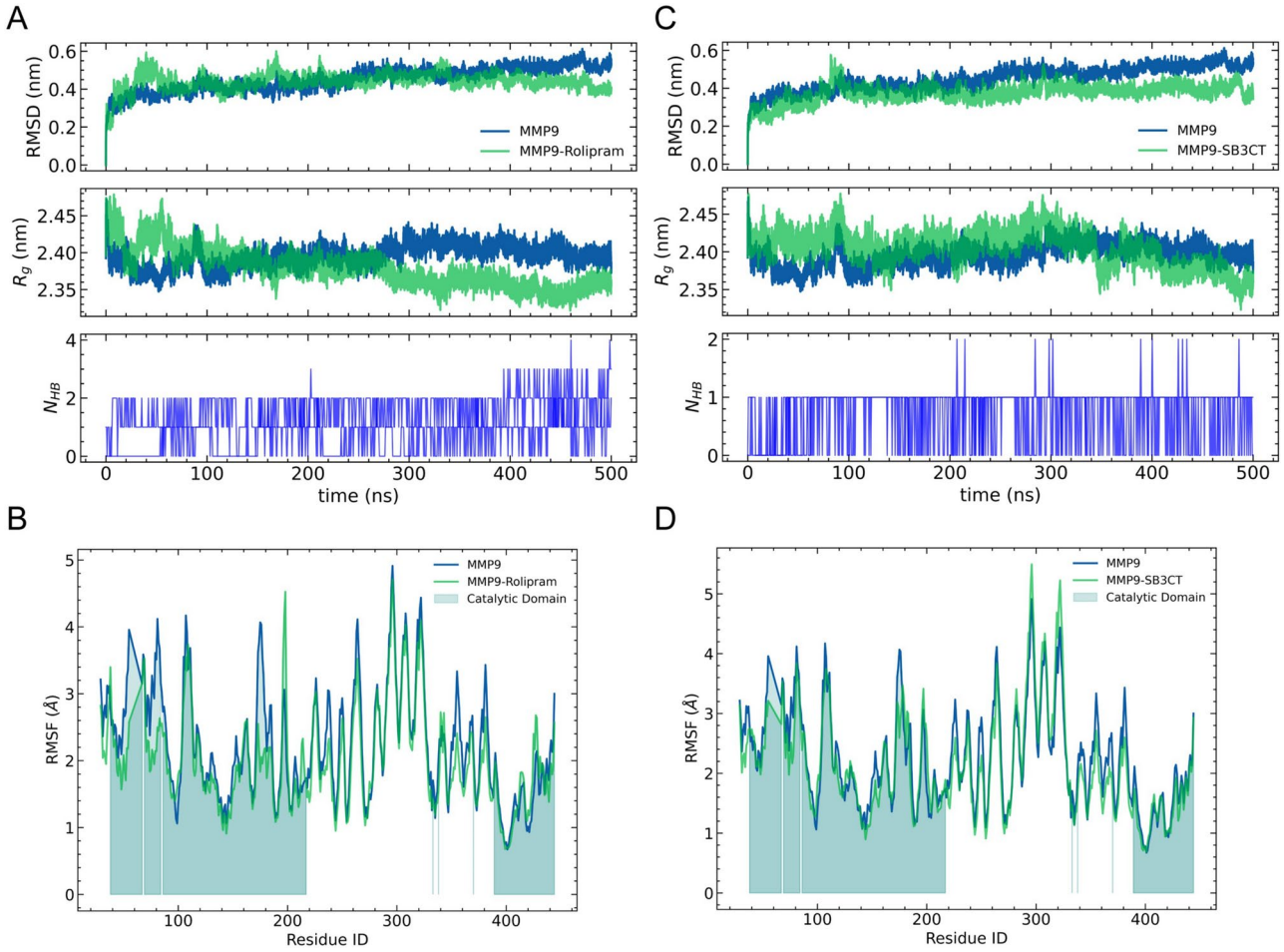

Fig. 7. (**A**) The RMSD plots (top panel) and radius of gyration (R_g) plots (middle panel) of free MMP9 and MMP9-rolipram complex, as well as the time plots of the number of hydrogen bonds (bottom panel) between MMP9 and rolipram that were detected by MDTraj. (**B**) RMSF plots of MMP9-rolipram complex with respect to free MMP9, for 500 ns of simulation time each. (**C**) The RMSD plots (top panel) and radius of gyration (R_g) plots (middle panel) of free MMP9 and MMP9-SB3CT complex, as well as the time plots of the number of hydrogen bonds (bottom panel) between MMP9 and SB3CT that were detected by MDTraj. (**D**) RMSF plots of MMP9-SB3CT complex with respect to free MMP9, for 500 ns of simulation time each.

Identification and examination of the stability of hydrogen bonds between rolipram and SB3CT with MMP9

Analysis of the hydrogen bonds between MMP9 and rolipram, following the Baker-Hubbard method revealed multiple positives in the catalytic domain with occurrences of more than 0.1 of the simulation time. However, further analysis of r_{ha} and θ_{dha} revealed that most of them were too intermittent or inconsistent in triplicate runs, leaving only two relatively steady hydrogen bonds with a frequency greater than 0.1. Only the hydrogen bonds involving the 188^{th} LEU and 189^{th} ALA amino acid residues were stable nearly throughout the entire simulation period, while the hydrogen bonds involving 99^{th} CYS and 424^{th} ARG formed after 200 ns (Fig. 6C and Fig. S4). In the control simulation with SB3CT, the Baker-Hubbard method identified only one hydrogen bond that was sufficiently persistent throughout the simulation time and consistent throughout the triplicates, namely the $N - H \cdots O$ hydrogen bond between the ligand and the 424^{th} ARG residue of MMP9 (Fig. 6D and Fig. S5).

PCA of the MMP9-rolipram and MMP9-SB3CT complexes

Trajectory files derived from MD simulations of the MMP9-rolipram and MMP9-SB3CT complexes were subjected to Principal Component Analysis (PCA). Detailed methodologies for PCA are outlined in Section Molecular dynamic simulation.

The results, plotted in Fig. 8 (rolipram) and Fig. 9 (SB3CT), reveal Free-Energy Landscapes (FEL) that exhibit several similarities with those obtained from the MMP2 simulations. Similarly to MMP2 complexes, the dynamics of the system is predominantly confined to a localized region of the principal component plane, with a discernible thermodynamic transition from a metastable minimum representing the initial state to a neighboring global minimum, presumed to be the final binding site where the hydrogen bonds described in

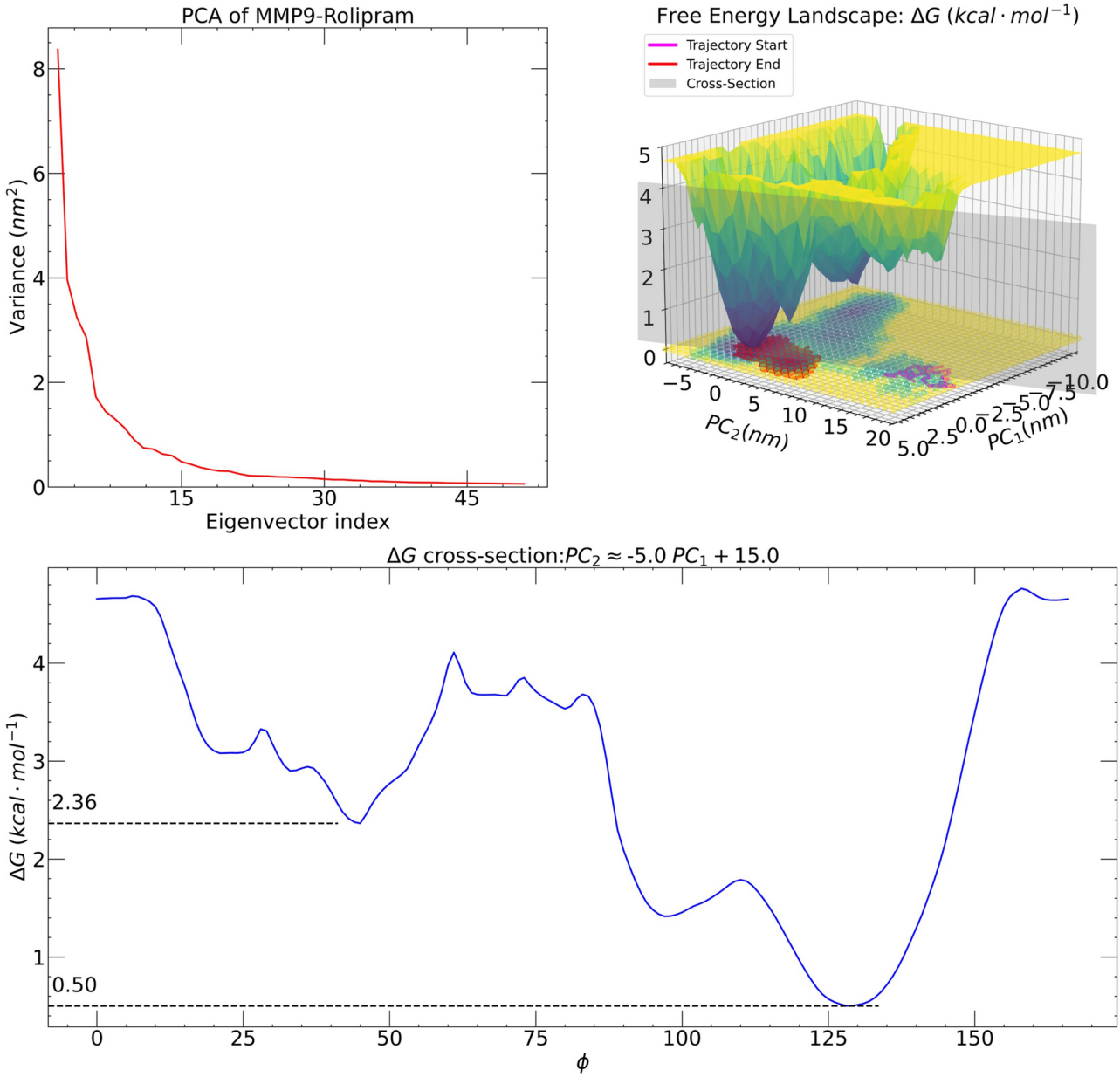

Fig. 8. PCA results for the MMP9-rolipram complex. The top left panel displays the eigenvalues plotted against the eigenvector index. The top right panel shows the free-energy landscape along the principal components $PC_{1,2}$ in a manner similar to the corresponding panel in Fig. 4. The bottom panel provides a cross-section of the landscape (also indicated in the top right panel) along a co-ordinate ϕ. Additionally, the free-energy estimates (in $kcal \cdot mol^{-1}$) at the two minima are indicated.

Section Identification and examination of the stability of hydrogen bonds between rolipram and SB3CT with MMP9 are persistent. These regions are distinct, yet proximate to the initial pose.

The confined regions are comparable in size for the MMP9-rolipram and MMP9-SB3CT dynamics, suggesting a similar protein response to each ligand, consistent with the conclusions of the hydrogen bond analysis as discussed in Section Identification and examination of the stability of hydrogen bonds between rolipram and SB3CT with MMP9. The lower panel cross-sections of the FEL provide a more distinct elucidation of these transitions. In both cases, thermal excitations move the system away from the metastable minimum and eventually into the global minimum, where the ligand is stably bound to the protein. The free-energy estimates at the two minima are also indicated in the

plots. The net change in free energy as the system transitions from initial to final equilibrium configuration is $\Delta G \approx -1.86\ kcal \cdot mol^{-1}$ ($\Delta G \approx -11.97\ kcal \cdot mol^{-1}$ from docked pose) for the MMP9-rolipram complex and $\Delta G \approx -1.53\ kcal \cdot mol^{-1}$ for the MMP9-SB3CT complex. The $\Delta G \approx -11.79\ kcal \cdot mol^{-1}$ from the docked pose is very close to the MMP9-rolipram complex, suggesting that rolipram inhibits MMP9 in a way that is qualitatively and quantitatively similar to the well-known inhibitor SB3CT.

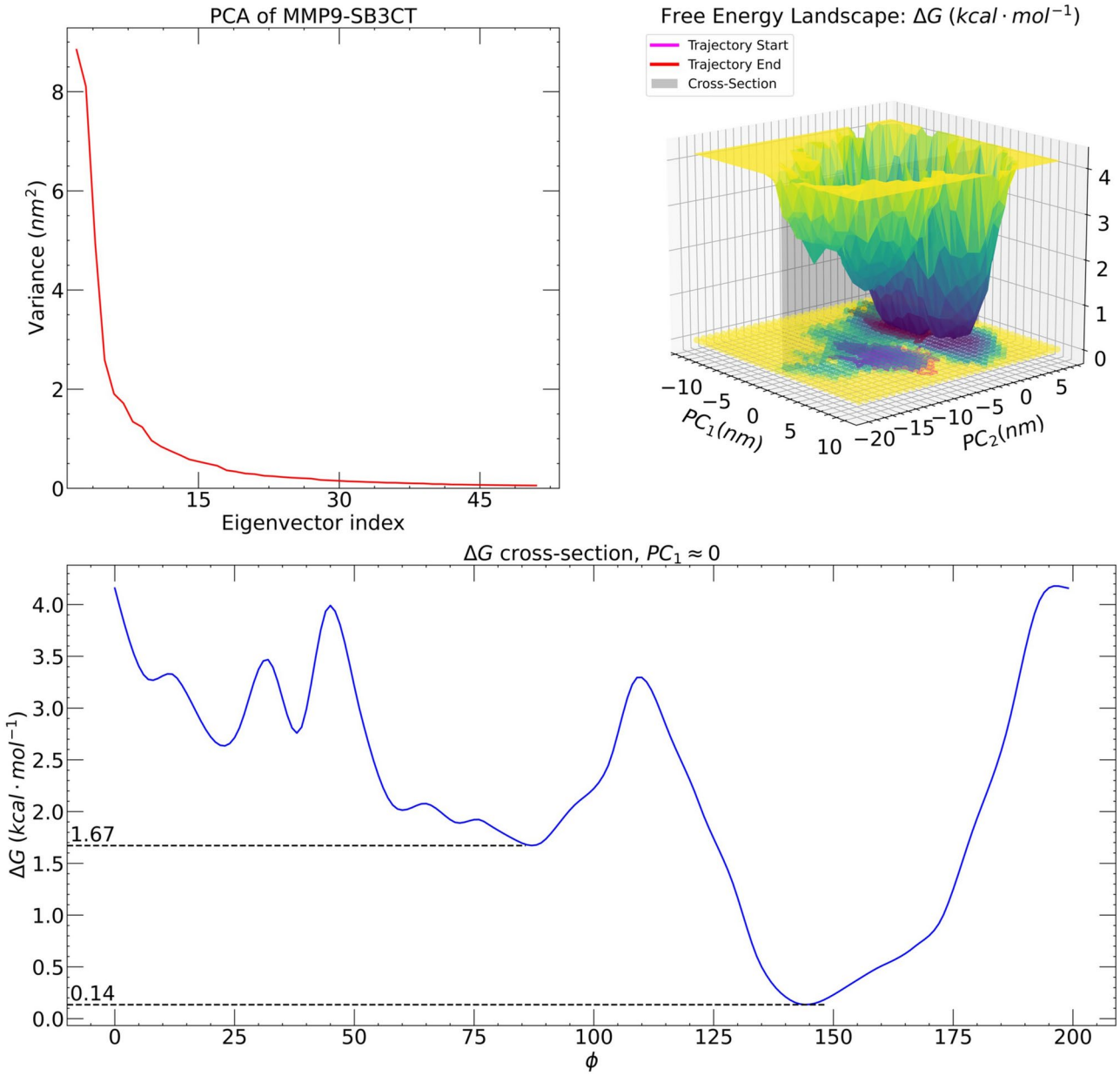

Fig. 9. PCA results for the MMP9-SB3CT complex showing eigenvalues plotted against eigenvector index in the top left panel. The top right panel shows the free energy landscape along the principal components in a manner similar to Fig. 4. The bottom panel shows the cross-section of the landscape along ϕ coordinate. The free energy estimates at the two minima are also indicated in $kcal \cdot mol^{-1}$.

Thus, the PCA analysis strongly indicates that rolipram inhibits MMP9 by forming hydrogen bonds with the 424^{th} ARG residue in the catalytic domain in a manner that is both qualitatively and quantitatively akin to the well-known inhibitor SB3CT.

Rolipram inhibited gelatinase activity of MMP2 and MMP9 in primary cells of breast cancer patients

Following the simulations of the computational models, the interaction of rolipram with MMP2 and MMP9 was further substantiated by gelatin zymography of culture media conditioned with primary cells of tumors of patients with breast cancer. The conditioned media of the primary tissue cultures were collected and incubated with rolipram at concentrations of 20 and 40 μM, each for 3 hours. Since the culture medium was already devoid of cells prior to rolipram treatment, the application of the PKA inhibitor H89 was not necessary to validate the activity of rolipram. Zymography showed that the enzymatic activities of MMP2 or MMP9 were not exerted on gelatin in the presence of rolipram, while both MMPs were able to exert their enzymatic activities in the absence of rolipram (Fig. 10).

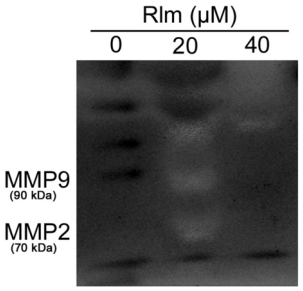

Fig. 10. Gelatin zymography of culture media conditioned with primary cells from human breast tumor tissue. The conditioned media were incubated with 20 and 40 μM concentrations of rolipram for 3 hours before zymography. The full-length gel image is available at Fig. S6.

Discussion

A previous investigation (available at[12]) demonstrated that rolipram negatively affected cell migration and scratch wound healing through hedgehog signaling dependent on the cAMP-PKA and cAMP-PKA / PI3K-Akt signaling pathways. Rolipram showed modulations in intracellular levels of MMP2 and MMP9, which are known to be associated with cell migration and metastatic potential of cells. However, cAMP-PKA-dependent modulations of MMP2 / 9 expression levels could not conclusively demonstrate the enzyme activities of these proteins. To further explore whether the regulation of MMP2 and MMP9 activities was solely dependent on cAMP-PKA (as apparently thought from studying the expression profiles of MMP2 and MMP9), gelatin zymography was performed with rolipram after co-administration of H89, a potent inhibitor of PKA. The results of the zymography analysis showed that rolipram effectively suppressed the gelatinase activity of MMP2 and MMP9 even in the presence of H89, challenging the previous assumption that such modulations depended on cAMP-PKA. This outcome suggested the possible potential of rolipram to influence MMPs by circumventing the cAMP-PKA-mediated signaling cascade. Rolipram was screened for potential off-target effects, revealing that some specific proteases, such as MMPs, were prominent in the screening results, along with its primary targets, PDEs.

Based on this prediction, possible interactions between rolipram and MMP proteins *in silico* were investigated. Molecular docking studies demonstrated significant binding affinities of rolipram with MMP2 and MMP9, similar to the control ligand, SB3CT, which is known to be a potent inhibitor of both MMP2 and MMP9. To further support the hypothesis that rolipram interacts with MMP2 and MMP9, MD simulations of the best-docked complexes were performed. The simulation results offered valuable information on the likely interaction of rolipram with MMP2 and MMP9. Both proteins, in their free state or in the presence of rolipram, remained stable and compact throughout the simulation period, mirroring the control simulation with SB3CT. During simulations, rolipram was observed to shift its initial docked position with MMP2 and establish a stable hydrogen bond. In the case of MMP9, rolipram formed multiple stable hydrogen bonds adjacent to the initial docked configuration. As expected, SB3CT also showed stable hydrogen bond formation with both proteins throughout the simulation, along with noticeable deviations from the initial docked conformations. Both the hydrogen bond analysis and the PCA results indicated that rolipram inhibits MMP9 more effectively than MMP2. The data also suggested that rolipram interacts with MMP2 and MMP9 in a manner similar to SB3CT. Therefore, the results of the MD simulations of these complexes provided improved insights into the functioning of rolipram, a PDE4 inhibitor.

Furthermore, when rolipram was added to the conditioned medium of primary cells obtained from human breast cancer patients, it inhibited the enzymatic activities of MMP2 and MMP9. The conditioned medium was incubated with 20 and 40 μM concentrations of rolipram. Because this medium was cell-free, it was evident from the result that rolipram's effect on the activities of these MMPs was independent of the cAMP-PKA signaling pathway that affects cancer cells in the primary culture. Although we have shown the inhibitory potential of rolipram on proteins such as MMP2 and MMP9 in this study, which are mainly consistent with zymography data, additional studies with a specific substrate of MMP 2 / 9 are required. In addition, wet lab data showing the interaction between purified and recombinant MMPs and rolipram would have strengthened the merit of the study.

However, the findings of this study show a possible off-target of the PDE4 inhibitor rolipram, suggesting its potential as a promising option for breast cancer therapy targeting proteins that are potent markers of metastasis.

Methods

Ethics statement

No animals were used in this study. Human breast cancer tissue samples were collected from the All India Institute of Medical Sciences (AIIMS) Kalyani, Kalyani, Nadia, West Bengal, India. The method of collection of samples was strictly in compliance with the guidelines of the Institutional Human Ethics Committee of AIIMS Kalyani. All experimental procedures, which involved patient samples, were also approved by the Institutional Human Ethics Committee of AIIMS Kalyani.

Materials

The estrogen and progesterone receptor positive human breast cancer cell line MCF-7 and the triple negative human breast cancer cell line MDA-MB-231 were purchased from the National Center for Cell Sciences (NCCS), Pune, India. The PDE4 inhibitor, Rolipram, was purchased from Sigma-Aldrich (USA, Cat # R6520) and a stock solution of 10 mM was prepared by dissolving it in ethanol. PKA inhibitor H89 was also purchased from Sigma-Aldrich (USA, Cat # B1427) and dissolved in DMSO to prepare a stock solution of 1 mM. Dulbecco's modified eagle medium (DMEM, Cat # 11885084), DMEM-F12 GlutaMAX^{TM} (Cat # 10565018), fetal bovine serum (FBS, United States, Cat # 16140071), penicillin-streptomycin (Cat # 15140122) were purchased from Gibco^{TM} (USA).

Cell culture and treatment

Human breast cancer cell lines were maintained in a culture medium consisting of DMEM, supplemented with 10% FBS and 100 U/ml penicillin-streptomycin. The cells were kept in a humidified atmosphere 5% CO_2 at $37^{\circ}C$. Cells were checked for the presence of any contaminants before any experiment and allowed to attain at least 70% confluence[16]. The MCF-7 and MDA-MB-231 cells were treated with concentrations of 40 μM and 53 μM rolipram, respectively.[12] for 24 hours. 10 μM[11] concentration of H89 was also used to treat these cell lines separately and in combination with previously mentioned doses of rolipram.

Primary tissue culture from human breast tumor tissue

The human breast tumor tissue samples were obtained from AIIMS Kalyani after receiving informed consent from patients according to the AIIMS Institutional Human Ethical Committee guidelines. The tissues were obtained from Tru-cut biopsy of the patients that were authenticated to be breast cancer by trained pathologists. The samples were washed with antibiotics (100 U/ml penicillin, 100 µg/ml streptomycin) and incubated with the collagenase-hyaluronidase mixture for $16-18$ $hours$ at $37^{\circ}C$ before being kept in a culture medium composed of DMEM/F-12 GlutaMAX^{TM}, supplemented with 10% FBS, $5\mu g/ml$ insulin and $0.5\mu g/ml$ hydrocortisone. For gelatin zymography, cells were kept in a serum-free culture medium for 12 $hours$ before collecting the culture medium, which was then equally divided into three microcentrifuge tubes. Two of these samples were incubated with 20 μM and 40 μM concentrations of rolipram for 3 $hours$ at $37^{\circ}C$ prior to the gelatin zymography study, while no rolipram was added to the other sample.

Gelatin zymography

Gelatin zymography in MCF7 and MDA-MB-231 involved cell culture medium conditioned by human breast cancer cell lines treated with rolipram, H89, and co-treatment of H89 and rolipram for 24 $hours$. Gelatin zymography was also performed with culture medium conditioned with primary cells from tumor tissues from human breast cancer patients, incubated with two different doses of rolipram for 3 $hours$, after collecting the cell-free medium. These samples were first resolved using a non-reducing 10% polyacrylamide gel, containing 1 mg/ml gelatin. The gels were washed twice with 2.5% Triton^{TM} X-100 (30 $minutes$ each) and incubated with incubation buffer for 24 $hours$ at $37^{\circ}C$. The incubation buffer, also known as the calcium assay buffer, is made up of 40 mM Tris-HCl (pH 7.4), 0.2 M NaCl, 10 mM $CaCl_2$ and NaN_3. Following incubation, the gels were stained with Coomassie blue 0.1% followed by destaining. Gel images were obtained from the Bio-Rad ChemiDoc XRS + System, using Bio-Rad Image Lab software, and zymographic band quantification was performed using the NIH ImageJ software[17,18].

Drug target prediction

The canonical Simplified Molecular Input Line Entry System (SMILES) format of rolipram was obtained from PubChem[19] and provided to the SwissTargetPrediction server[20] to predict probable protein targets of rolipram.

Molecular docking

The molecular structures of the MMP2 and MMP9 proteins were obtained from the Protein Data Bank (PDB) from the website www.rcsb.org. The 3D coordinates of the ligands, rolipram and 2-[(4-phenoxyphenyl) sulfonylmethyl]thiirane (SB3CT) were obtained from PubChem[19,21] in the format of a structured data file (SDF). These coordinates were then converted to the PDB format using Open Babel[22]. To perform the computational molecular docking of MMP2 and MMP9 with rolipram and SB3CT, Autodock-Zn was used in AMDock (version 1.6.x for Linux)[23]. The structures of the MMP2 and MMP9 proteins, as well as the rolipram and SB3CT ligands, were provided as separate PDB files to AMDock. The input was prepared by loading the force field data using the CHARMM force field model[24], hydrogen topology data, and updated disulfide bridge data. No repairs were needed during this process. After input preparation, the search space was defined in the catalytic domains of each protein. Then, the Autodock tool was instructed to perform independent docking simulations. Finally, the output, which included the final poses of the protein-ligand complexes and their binding affinity in kilocalories per mole (*kcal/mol*), was recorded in the PDB files. To analyze the results, the protein-ligand interaction surfaces were visualized using PyMOL[25] and LigPlot^{+}[26].

Molecular dynamic simulation

Molecular dynamics (MD) simulations were performed using `GROMACS` (version 2022.4)[27–29] to study the behavior of protein-ligand complexes. The simulations were carried out on a Terascale High-Performance Computing Cluster at the S.N. Bose Innovation Centre, University of Kalyani, Kalyani, India. `GROMACS` is a versatile molecular dynamics simulation package that can simulate complex biomolecules in virtual environments that mimic laboratory conditions. The molecular coordinates of the MMP2 and MMP9 proteins were converted to the appropriate simulation formats using internal `GROMACS` tools, as well as the CHARMM force field[24]. The ligands, rolipram and SB3CT, were generated using the SwissParam server[20]. The molecular coordinates of the

proteins and ligands, along with solvent water molecules (whose microscopic chemistry was treated using the flexible simple point-charge water model) and charge-neutralizing ions, were combined to create a configuration file for each protein-ligand complex. The configuration file was combined with the force field parameters and the external bath couplings (to achieve thermal equilibrium under laboratory conditions) to form a topology file that was fed to the `GROMACS` MD trajectory builder. Subsequently, `GROMACS` was instructed to randomly draw atom velocities from a Maxwell-Boltzmann distribution at room temperature and simulate the ensuing dynamics using the leapfrog numerical integration technique.

Thus, `GROMACS` was able to successfully generate trajectory files that captured the temporal dynamics of the atoms. These trajectory files were then analyzed using the `GROMACS` internal tools and the `MDAnalysis` Python module[30]. The stability and integrity of each protein-ligand complex were individually evaluated by calculating the root-mean-square deviation (RMSD) of the protein backbone from its initial configuration and the radius of gyration (R_g) of the protein backbone throughout the simulation[31]. To assess structural fluctuations resulting from protein-ligand interactions, root-mean-square fluctuations (RMSF) of the amino acid residues of the proteins were calculated. Higher RMSF values indicate regions with greater structural mobility. The data represented in the figures are the arithmetic mean of three independent simulations. The stability and characteristics of the protein-ligand interaction were also validated by analyzing the formation of hydrogen bonds. The number of hydrogen bonds formed during the simulation was determined using the `MDTraj` Python module [14]. `MDTraj` was also utilized to determine the distance and angle between the atoms involved in the formation of hydrogen bonds over time.

Finally, data from the Principal Component Analysis (PCA) were obtained using `GROMACS` [32]. The PCA identified the dominant correlations in the protein-ligand complex dynamics by extracting and projecting the trajectory along the directions (labeled PC_1 and PC_2) of the eigenvectors corresponding to the two largest eigenvalues of the covariance matrix, as described by elements [33]:

$$C_{ij} = \left\langle M_{ii}^{1/2}\left(x_i - \langle x_i \rangle\right)\, M_{jj}^{1/2}\left(x_j - \langle x_j \rangle\right) \right\rangle. \tag{1}$$

Here, $x_{i,j}(t)$ are the time-varying atomic coordinates (backbone, ligand and Zinc ion selections only), and M represents the diagonal atomic mass matrix of the selected atoms. The notation $\langle \cdots \rangle$ signifies time-averages over the entire trajectory. The covariance matrix was obtained and diagonalized using the `gmx covar` subprogram in `GROMACS`. The eigenvector data was used to project the trajectory in the plane spanned by the principal axes using the `gmx anaeig` subprogram, and the resultant data points were binned into a histogram and Boltzmann-inverted by the `gmx sham` subprogram [32] to obtain a Free Energy Landscape (FEL). The landscape data was then interpolated into a bicubic spline using the `SciPy` library [34] to obtain a continuous representation of the FEL. Whenever the structure of the FEL revealed a thermodynamic transition from a metastable minimum proximate to the initial state of the simulation (in the vicinity of the docked configuration) to a global minimum near the final state at the end of the simulation, a cross-section of the spline was sampled along the co-ordinate ϕ that lay along the line joining the two regions in the principal component plane. The free energy difference between the two minima was utilized as an estimate of the free energy change during the thermodynamic transition. These minima were determined numerically using the `SciPy` wrapper for Powell's dog-leg method [35], applied to the cross-section of the spline. In all instances, the change in free energy was subsequently added to the initial binding affinity observed in the docked pose to derive the final change in free energy.

Data availability

All data supporting the findings of the study are available from the corresponding authors upon request.

Received: 23 May 2024; Accepted: 21 March 2025
Published online: 31 March 2025

References

1. Chen, J.-S. et al. Sonic hedgehog signaling pathway induces cell migration and invasion through focal adhesion kinase/AKT signaling-mediated activation of matrix metalloproteinase (MMP)-2 and MMP-9 in liver cancer. *Carcinogenesis* **34**, 10–19. https://doi.org/10.1093/carcin/bgs274 (2013).
2. Vihinen, P., Ala-aho, R. & Kähäri, V.-M. Matrix metalloproteinases as therapeutic targets in cancer. *Curr. Cancer Drug Targets* **5**, 203–220. https://doi.org/10.2174/1568009053765799 (2005).
3. Freije, J. M. P. et al. Matrix metalloproteinases and tumor progression. *Adv. Exp. Med. Biol.* **532**, 91–107. https://doi.org/10.1007/978-1-4615-0081-0_9 (2003).
4. Ahmad, S., Singh, V., Sinha, R. J., Srivastava, A. & Mandhani, A. Role of MMP-2, MMP-9 and VEGF as serum biomarker in early prognosis of renal cell carcinoma. *Afr. J. Urol.* **24**, 255–263. https://doi.org/10.1016/j.afju.2018.09.003 (2018).
5. Benitha, G. et al. Evaluation of Serum Levels of Matrix MetalloProteinase-9 (MMP-9) in Oral Squamous Cell Carcinoma and Its Clinicopathological Correlation. *Cureus* **15**, e34954. https://doi.org/10.7759/cureus.34954 (2023).
6. Li, H., Qiu, Z., Li, F. & Wang, C. The relationship between MMP-2 and MMP-9 expression levels with breast cancer incidence and prognosis. *Oncol. Lett.* **14**, 5865–5870. https://doi.org/10.3892/ol.2017.6924 (2017).
7. Jiang, H. & Li, H. Prognostic values of tumoral MMP2 and MMP9 overexpression in breast cancer: a systematic review and meta-analysis. *BMC Cancer* **21**, 149. https://doi.org/10.1186/s12885-021-07860-2 (2021).
8. Muniz-Bongers, L. R. et al. MMP2 and TLRs modulate immune responses in the tumor microenvironment. *JCI Insight* **6**, e144913. https://doi.org/10.1172/jci.insight.144913 (2021).
9. Leifler, K. S. et al. Inflammation induced by MMP-9 enhances tumor regression of experimental breast cancer. *J. Immunol. Author Choice* **190**, 4420–4430. https://doi.org/10.4049/jimmunol.1202610 (2013).

10. Sakkas, L. I., Mavropoulos, A. & Bogdanos, D. P. Phosphodiesterase 4 inhibitors in immune-mediated diseases: Mode of action, clinical applications, current and future perspectives. *Curr. Med. Chem.* https://doi.org/10.2174/0929867324666170530093902 (2017).
11. Mukherjee, P. et al. PDE4 inhibitor eliminates breast cancer stem cells via noncanonical activation of mTOR. *J. Cell. Biochem.* **123**, 1980–1996. https://doi.org/10.1002/jcb.30325 (2022).
12. Bagchi, A., Bhattacharya, A., Chatterji, U. & Biswas, A. PDE4 inhibitor rolipram represses hedgehog signaling via ubiquitin-mediated proteolysis of gli transcription factors to regress breast cancer. *bioRxiv* https://doi.org/10.1101/2024.03.03.583221 (2024).
13. Hashimoto, H. et al. Structural Basis for Matrix Metalloproteinase-2 (MMP-2)-selective Inhibitory Action of β-Amyloid Precursor Protein-derived Inhibitor. *J. Biol. Chem.* **286**, 33236–33243. https://doi.org/10.1074/jbc.M111.264176 (2011).
14. McGibbon, R. T. et al. Mdtraj: A modern open library for the analysis of molecular dynamics trajectories. *Biophys. J* . **109**, 1528–1532. https://doi.org/10.1016/j.bpj.2015.08.015 (2015).
15. Rowsell, S. et al. Crystal Structure of Human MMP9 in Complex with a Reverse Hydroxamate Inhibitor. *J. Mol. Biol.* **319**, 173–181. https://doi.org/10.1016/S0022-2836(02)00262-0 (2002).
16. Bhaduri, R. et al. Cytotoxic activity of nitrogen, sulfur, and oxygen chelated Pt(II) complexes; their DNA/BSA binding by in vitro and in silico approaches. *J. Mol. Liq.* **360**, 119529. https://doi.org/10.1016/j.molliq.2022.119529 (2022).
17. Rudra, D. S., Pal, U., Maiti, N. C., Reiter, R. J. & Swarnakar, S. Melatonin inhibits matrix metalloproteinase-9 activity by binding to its active site. *J. Pineal Res.* **54**, 398–405. https://doi.org/10.1111/jpi.12034 (2013).
18. Toth, M., Sohail, A. & Fridman, R. Assessment of gelatinases (MMP-2 and MMP-9) by gelatin zymography. *Methods Mol. Biol. (Clifton N.J.)* **878**, 121–135. https://doi.org/10.1007/978-1-61779-854-2_8 (2012).
19. National Center for Biotechnology Information. "PubChem Compound Summary for CID 5092, Rolipram" *PubChem*,. https://pubchem.ncbi.nlm.nih.gov/compound/5092 Accessed 20 March, 2024.
20. Zoete, V., Cuendet, M. A., Grosdidier, A. & Michielin, O. SwissParam: a fast force field generation tool for small organic molecules. *J. Comput. Chem.* **32**, 2359–2368. https://doi.org/10.1002/jcc.21816 (2011).
21. National Center for Biotechnology Information. "PubChem Compound Summary for CID 9883002, 2-[(4-Phenoxyphenyl) sulfonylmethyl]thiirane" *PubChem*,. https://pubchem.ncbi.nlm.nih.gov/compound/2-_4-Phenoxyphenyl_sulfonylmethyl_thiirane (2024).
22. O'Boyle, N. M. et al. Open Babel: An open chemical toolbox. *J. Cheminform.* **3**, 33. https://doi.org/10.1186/1758-2946-3-33 (2011).
23. Tresanco, M. S. V. AMDock: Assisted Molecular Docking with Autodock4 and Autodock Vina. Original-date: 2018-02-20T16:41:39Z (2023).
24. MacKerell, A. D. et al. All-atom empirical potential for molecular modeling and dynamics studies of proteins. *J. Phys. Chem. B* **102**, 3586–3616. https://doi.org/10.1021/jp973084f (1998).
25. Schrödinger, L. The PyMOL molecular graphics system, version 1.8 (2015). https://pymol.org.
26. Laskowski, R. A. & Swindells, M. B. LigPlot+: Multiple Ligand-Protein Interaction Diagrams for Drug Discovery. *J. Chem. Inf. Model.* **51**, 2778–2786. https://doi.org/10.1021/ci200227u (2011).
27. Lindahl, E. R. Molecular dynamics simulations. *Methods Mol. Biol. (Clifton N. J.)* **443**, 3–23. https://doi.org/10.1007/978-1-59745-177-2_1 (2008).
28. Páll, S., Abraham, M. J., Kutzner, C., Hess, B. & Lindahl, E. Tackling Exascale Software Challenges in Molecular Dynamics Simulations with GROMACS. In *Solving Software Challenges for Exascale, Lecture Notes in Computer Science* (eds Markidis, S. & Laure, E.) 3–27 (Springer International Publishing, 2015). https://doi.org/10.1007/978-3-319-15976-8_1.
29. Abraham, M. J. et al. GROMACS: High performance molecular simulations through multi-level parallelism from laptops to supercomputers. *SoftwareX* **1–2**, 19–25. https://doi.org/10.1016/j.softx.2015.06.001 (2015).
30. Michaud-Agrawal, N., Denning, E. J., Woolf, T. B. & Beckstein, O. MDAnalysis: a toolkit for the analysis of molecular dynamics simulations. *J. Comput. Chem.* **32**, 2319–2327. https://doi.org/10.1002/jcc.21787 (2011).
31. Lemkul, J. A. From proteins to perturbed hamiltonians: A suite of tutorials for the GROMACS-2018 molecular simulation package [Article v1.0]. *Liv. J. Computat. Mol. Sci.* **1**, 5068–5068. https://doi.org/10.33011/livecoms.1.1.5068 (2019).
32. Al-Khafaji, K. & Taskin Tok, T. Molecular dynamics simulation, free energy landscape and binding free energy computations in exploration the anti-invasive activity of amygdalin against metastasis. *Comput. Methods Programs Biomed.* **195**, 105660. https://doi.org/10.1016/j.cmpb.2020.105660 (2020).
33. Amadei, A., Linssen, A. B. M. & Berendsen, H. J. C. Essential dynamics of proteins. *Proteins Struct. Funct. Bioinform.* **17**, 412–425. https://doi.org/10.1002/prot.340170408 (1993).
34. Fundamental Algorithms for Scientific Computing in Python. Virtanen, P. et al. SciPy 1.0. *Nat. Methods* **17**, 261–272. https://doi.org/10.1038/s41592-019-0686-2 (2020).
35. Powell, M. A new algorithm for unconstrained optimization. In *Nonlinear Programming* (eds Rosen, J. et al.) 31–66 (Academic Press, 1970).

Acknowledgements

The authors thank the Science & Engineering Board, Government of India [Grants SUR/2022/001275 and CRG/2018/004002], Department of Biotechnology, Government of West Bengal, India [No. 248 (Sanc)/BT (Estt)/RD-27/2016] for funding this study. The authors also thank the HPC Facility of the University of Kalyani, the DST-FIST and UGC-SAP programs of the Department of Zoology of the University of Kalyani, and the DST-PURSE-sponsored instrument facilities of the University of Kalyani for providing infrastructure facilities and the Personal Research Grant of the University of Kalyani.

Author contributions

A.BA. carried out all experiments and simulations. A.R. helped with HPC management and preparation of the simulation scripts. A.BI. and A.R. obtained funding, conceptualized the experiments, designed them, interpreted the data, and prepared the manuscript. A.H. provided the tru-cut biopsy sample of the breast cancer patient from which the primary cell culture was performed. All authors approve of this version of the manuscript as final.

Declarations

Competing interests

The authors declare no competing interests.

Additional information

Supplementary Information The online version contains supplementary material available at https://doi.org/10.1038/s41598-025-95549-y.

Correspondence and requests for materials should be addressed to A.R. or A.B.

Reprints and permissions information is available at www.nature.com/reprints.

Publisher's note Springer Nature remains neutral with regard to jurisdictional claims in published maps and institutional affiliations.